Effects of Porous Gap Fillers on 30P30N Leading-Edge Slat Noise. Part I: Surface Pressure and Acoustics

Yang Zhang* and Louis N. Cattafesta III†
Florida Center for Advanced Aero-Propulsion (FCAAP), Florida A&M University and Florida State University, Tallahassee, Florida, 32310, US

Meelan M. Choudhari,‡ Kyle A. Pascioni,§ Mehdi R. Khorrami,¶ David P. Lockard,‖ and Travis Turner**
NASA Langley Research Center, Hampton, VA, 23681, US

The leading edge slat of a high-lift system is one of the main contributors to airframe noise during approach. In a previous experimental study, we assessed the performance of an impermeable slat gap filler as a passive flow control device to reduce the slat noise associated with a two-dimensional, three-element high-lift airfoil. The present paper, the first of two parts, represents a follow-on investigation to assess the relative efficacy of permeable gap fillers that allow successively higher amounts of flow to pass through the gap. To evaluate the influence of this passive flow control device on the acoustics generated by the unsteady flow near the slat, experiments are conducted in an anechoic wind tunnel by mounting a gap filler to the slat element of the two-dimensional 30P30N high-lift configuration. Measurements are performed at a single geometric angle of attack ($\alpha_k = 8°$) and three different flow speeds that correspond to Reynolds numbers of $Re_c = 1.2 \times 10^6$, 1.5×10^6, and 1.71×10^6, respectively. Steady surface pressure measurements are used to gauge the influence of the permeable gap filler treatments on the overall lift. The effect of each treatment on the radiated noise is analyzed via acoustic array measurements, followed by delay-and-sum beamforming to locate the slat noise sources and to provide the integrated acoustic spectra. The porous gap fillers are found to eliminate the narrowband peaks in the acoustic spectra and, also, to yield a 10 dB reduction in the broadband noise in comparison with the baseline case with no gap filler. The porous gap filler with the lowest permeability acts similar to the impermeable gap filler examined previously. However, the aerodynamics and noise reduction both degrade with increasing permeability. An accompanying abstract describes the particle image velocimetry measurements of the flowfield within the slat cove and on either side of the permeable gap filler.

Nomenclature

C_l	=	sectional lift coefficient
C_p	=	pressure coefficient
c	=	stowed chord length of multielement airfoil configuration, m
f	=	frequency, Hz
p	=	static pressure, Pa
p_∞	=	freestream static pressure, Pa
q_∞	=	freestream dynamic pressure, Pa
Re_c	=	Reynolds number based on stowed chord length of multielement airfoil configuration and freestream speed
St_s	=	Strouhal number based on slat chord and freestream speed
s	=	slat chord length, m

*Research Faculty, Department of Mechanical Engineering, AIAA Member. yz12b@fsu.edu
†Professor and University Eminent Scholar, Department of Mechanical Engineering, AIAA Associate Fellow.
‡Aerospace Technologist, Computational AeroSciences Branch, AIAA Fellow.
§Research Aerospace Engineer, AIAA Member.
¶Aerospace Technologist, Computational AeroSciences Branch, AIAA Associate Fellow.
‖Aerospace Technologist, Computational AeroSciences Branch, AIAA Associate Fellow.
**Aerospace Technologist, Computational AeroSciences Branch, AIAA Associate Fellow.

U_∞ = freestream flow speed, m/s
x = streamwise direction, m
y = vertical direction, m
z = spanwise direction, m
α_k = angle of attack with respect to Kevlar wall, degrees

I. Introduction

DURING the landing phase, deployed high-lift devices and the landing gear contribute a significant portion of the total aircraft noise. Along with the trailing edge flaps, the leading edge slat is often the dominant contributor to the noise associated with the high-lift devices [1]. Slat noise generation mechanisms are complicated and have been studied for many years. Slat noise usually contains both broadband and narrowband characteristics, which represent the combined outcome of several flow-induced source mechanisms. Khorrami et al. [2] and Singer et al. [3] showed that the high frequency tonal noise ($20 < St_s < 40$) is caused by vortex shedding from the blunt trailing edge of the deployed slat. Khorrami et al. [4] and Choudhari et al. [5] found the interaction of the slat shear layer with the high-lift geometry to be responsible for the low-to-mid frequency broadband component. It is well accepted that the strong narrowband peaks in the mid-Strouhal range ($1 < St_s < 5$) in both the near field surface pressure spectra and the far-field acoustic spectra are linked to a flow-acoustic feedback of slat-cove shear layer instabilities [6, 7]. The generation of these peaks is analogous to the Rossiter modes [8] in the context of open cavity flows. Also, recent phase-locked PIV measurements suggest the presence of a bulk cove oscillation at a low Strouhal number ($St_s \approx 0.15$), which is related to the unsteady impingement location, i.e., slat-cove shear layer flapping [9]. Slat noise is also known to have a broadband component with a peak in the Strouhal range close to unity. Choudhari and Khorrami [10] attributed this to the surface impingement of the unsteady vortical structures convected along the slat cove shear layer; this mechanism has been corroborated by Knacke and Thiele [11] using statistical correlation techniques.

With the knowledge of the noise generation mechanisms, a number of studies have been performed to reduce the flow unsteadiness and/or weaken its interaction with the airfoil surfaces in order to suppress the noise radiation. The passive approaches can be grouped into three categories:

1) Modifying the slat cusp with serrations or an extension to reduce the disturbances in the shear layer [12–16]. This concept generally reduces the growth and/or spanwise coherence of the shear layer disturbances.
2) Filling the entire slat cove with a streamlined profile to minimize the flow separation [16–20]. With a streamlined geometry, the strong narrowband peaks induced by the shear layer disturbances no longer exist.
3) Reducing or sealing the gap between the slat and the main wing [16, 21–24]. This technique reduces the vortex shedding from the slat trailing edge and alters the reattachment point of the slat-cove shear layer.

The key requirement for an effective passive device is to significantly reduce the noise level (both broadband and narrowband) with minimal negative effects on the aerodynamics. Last but not least, the passive device should be simple, without adding too much additional weight or mechanical complexity to the wing or any obstructions to the retraction of the slat.

The current study expands our previous investigation [16, 25, 26] of passive noise reduction concepts for the slat. The earlier study evaluated the effectiveness of slat cusp extensions, a cove filler, and a solid gap filler treatment. Although both cove filler and gap filler are able to eliminate the narrowband peaks induced by the slat cove shear layer, the noise suppression mechanisms are different. The cove filler eliminated the flow separation over the cove, while the gap filler alters the shear layer trajectory. It should be noted that, the slat needs to be retracted during cruise. For this reason, the gap filler is easier to implement. The aeroacoustic performance of a deployable design of a solid, i.e., nonporous gap filler on a semispan model of a realistic high-lift configuration was measured during the CRM-HL wind tunnel experiment at the NASA Langley Research Center. Therefore, the concept of a gap filler is further investigated in the current study, in particular, by using different porous media to regulate the amount of flow through the gap interface as against the total blockage by the solid (i.e., impermeable) gap filler. The current study consists of two parts, 1) examination of steady/unsteady surface pressure and far-field acoustics; and 2) Particle Image Velocimetry (PIV) investigation of the flow field. Part I assesses the noise reduction effects of the different porous gap fillers, and part II studies the underlying physical mechanisms.

II. Experimental Setup

A. Wind tunnel facility and airfoil model

The experiments were conducted in the Florida State Aeroacoustic Tunnel (FSAT) facility located at the Florida Center for Advanced Aero-Propulsion (FCAAP) at the Florida State University (FSU) [27]. All of the tests in the current work were carried out in the test section with two Kevlar side panels. The schematic and the main dimensions of the two-dimensional airfoil model are provided in Figure 1 and Table 1, respectively. The test section dimensions in the streamwise, spanwise, and vertical directions correspond to L=2.74 m, W=1.22 m, and H=0.91 m, respectively. The 30P30N high-lift configuration employed during this work has been used extensively to provide validation data for the AIAA workshop series on Benchmark Problems for Airframe Noise Computations (BANC). An overview of this workshop series was given in Ref. [28], and Ref. [29] provides a description of the 30P30N slat noise configuration as well as a summary of the computational and experimental contributions from the BANC-III Workshop. The model is mounted vertically in the middle of the FSAT test section, spanning the full tunnel height at this location. To minimize any blockage effects due to the model, the static pressure is measured from a tap on the contraction floor farther upstream, and a correction is applied based on the area ratio associated with the contraction. Three different flow speeds (with chord-based Reynolds numbers of 1.2×10^6, 1.5×10^6, and 1.71×10^6) are selected as the test conditions in the current study. The fixed geometric angle of attack equal to 8° produces a steady C_p distribution on the airfoil centerline that is similar to the free-air (i.e., an infinite freestream) numerical simulations based on Menter's Shear Stress Transport (SST) turbulence model at 5.5° angle of attack [30]. Figure 1 shows two coordinate systems, in both of which x represents the streamwise direction, y is normal to the airfoil chord line, and z is along the airfoil span to make a right-handed system. The coordinate system indicated in red is used for PIV plots with its origin at the leading edge of the stowed airfoil; the coordinate system indicated in blue is used for Delay-and-Sum (DAS) source maps with the origin at the wing rotation point.

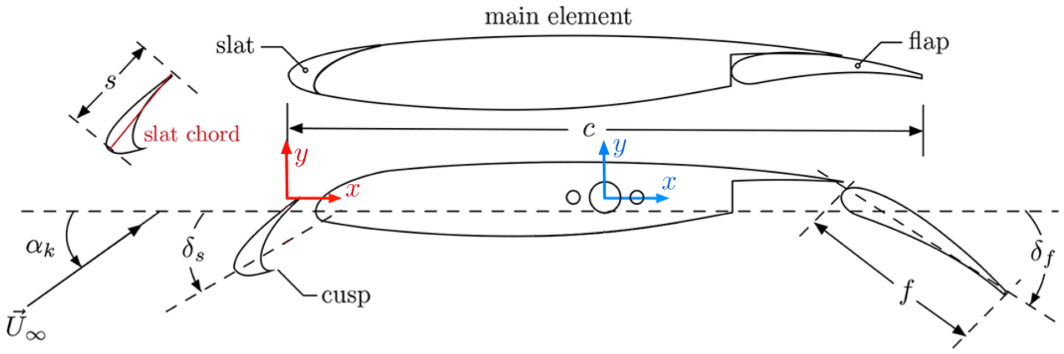

Fig. 1 Schematic of the 30P30N multielement airfoil.

Table 1 Primary dimensions of 30P30N airfoil.

Stowed chord	c	0.457 m
Span length	b	0.914 m
Slat chord	s	$0.15c$
Flap chord	f	$0.3c$
Slat deflection angle	δ_s	30°
Flap deflection angle	δ_f	30°

B. Porous gap fillers

The solid gap filler completely blocks the flow through the slat gap, thereby reducing the high speed flow around the main wing leading edge resulting in a reduction of local lift. In order to tune the amount of flow passing through the gap, porous media are mounted to a gap filler skeleton covering the gap between the slat and main wing. The porous gap

filler design follows the same profile as the solid gap filler. Due to the limitation of wire electrical discharge machining (EDM), the gap filler skeleton was divided into five 6-inch segments and two 3-inch segments at either end. The odd number of segments is required to avoid an impermeable joint at the center of the model. Two different views of the gap filler skeleton and main dimensions are provided in Figure 2. The skeleton is attached to the slat using 18 Philips head screws and glued to the main wing side by using J-B Weld Epoxy.

There are three different porous media samples with nominal thicknesses of 51 μm,737μm, and 533μm, respectively. The pictures of the samples are given in Figure 3 with reducing permeability from sample H to L. The nominal flow resistance of the samples are $0.08\rho_0 c_0$, $0.24\rho_0 c_0$, and $0.72\rho_0 c_0$, respectively. The porous media are attached to the skeleton one at a time on the pressure side by using a 3M™ VHB adhesive transfer tape. Because sample H is too thin and flexible to attach to the skeleton near the tail, this sample is extended to the trailing edge of the skeleton so that it is sandwiched between the skeleton and the main wing as shown in Figure 4a. Samples M and L are rigid enough to attach to the skeleton without deformation, as shown in Figure 4b. The residual glue during installation is cleaned, and a picture of installed sample H is given in Figure 4c.

C. Steady surface pressure

To help characterize the aerodynamic performance of the airfoil with and without the gap filler, the mean surface pressure on the high-lift configuration was measured at a total of 122 static pressure ports that are instrumented on the 30P30N model. These ports are distributed both chordwise and across the span at selected locations as shown in Figure 5. It should be noted that some of the pressure taps along the slat pressure surface and a few over the main wing leading edge are covered by the noise reduction devices as shown in Figure 2. Pressure scanners (Scanivalve DSA 3217) with multiple pressure ranges were used to acquire a total of 100 samples for each test condition at a sampling rate of 2 Hz. The 100 samples at each port were averaged to produce the steady pressure values. The coefficient of pressure is determined as $C_p = (p - p_\infty)/q_\infty$.

D. Unsteady pressure measurement

Kulite® unsteady pressure sensors are flush mounted on the slat to measure the local fluctuating pressures at different locations as shown in Table 2. Data from all sensors are simultaneously sampled at 204.8 kHz for 30 seconds for each Kulite using a NI PXI 1045 chassis and AC-coupled NI 4498 cards (24-bit). Welch's method is applied to calculate spectra using 16384 samples for the FFT with a Hanning window and 75% overlap in each block, resulting in a bin resolution of 12.5 Hz and a random uncertainty of 3.6% in spectral amplitude. It should be noted that P_2 is bad, and P_4 and P_5 are covered by the gap filler as shown in Figure 2.

Table 2 Locations of Kulite surface pressure sensors.

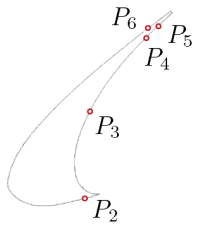

	x/c	y/b	z/c
P_2	-0.0379	-0.0346	-0.1119
P_3	-0.0336	-0.0346	-0.0578
P_4	0.0058	-0.0346	-0.0070
P_5	0.0115	-0.0346	-0.0017
P_6	0.0067	-0.0346	-0.0020

E. Far-field acoustic measurement

A phased microphone array comprised of a combination of fifty-five 1/4-inch GRAS.40BE and Brüel and Kjær 4958 free field microphones were used to measure the far-field acoustic signals that were used to allow source localization via beamforming. The microphone layout was optimized via numerical simulations of the Point Spread Function (PSF) [31], and it has a log-spiral pattern as shown in Figure 6. The frame that holds the microphones is designed to minimize acoustic reflections. It is an aluminum skeleton frame that was fabricated via a waterjet cutting process and it is covered by 76 mm foam wedges, not shown in the figure. Each microphone is held away from the aluminum frame by a 0.15 m long steel rod in order to minimize any acoustic reflections and the near field scattering effects [7]. It is located at a distance of 1.2 m from the surface of the airfoil position at $\alpha_k = 0°$ and is centered on the axis of rotation of the airfoil at $x = 0.5c$ with respect to the stowed leading edge as shown in Figure 7. The microphone array faces the pressure side

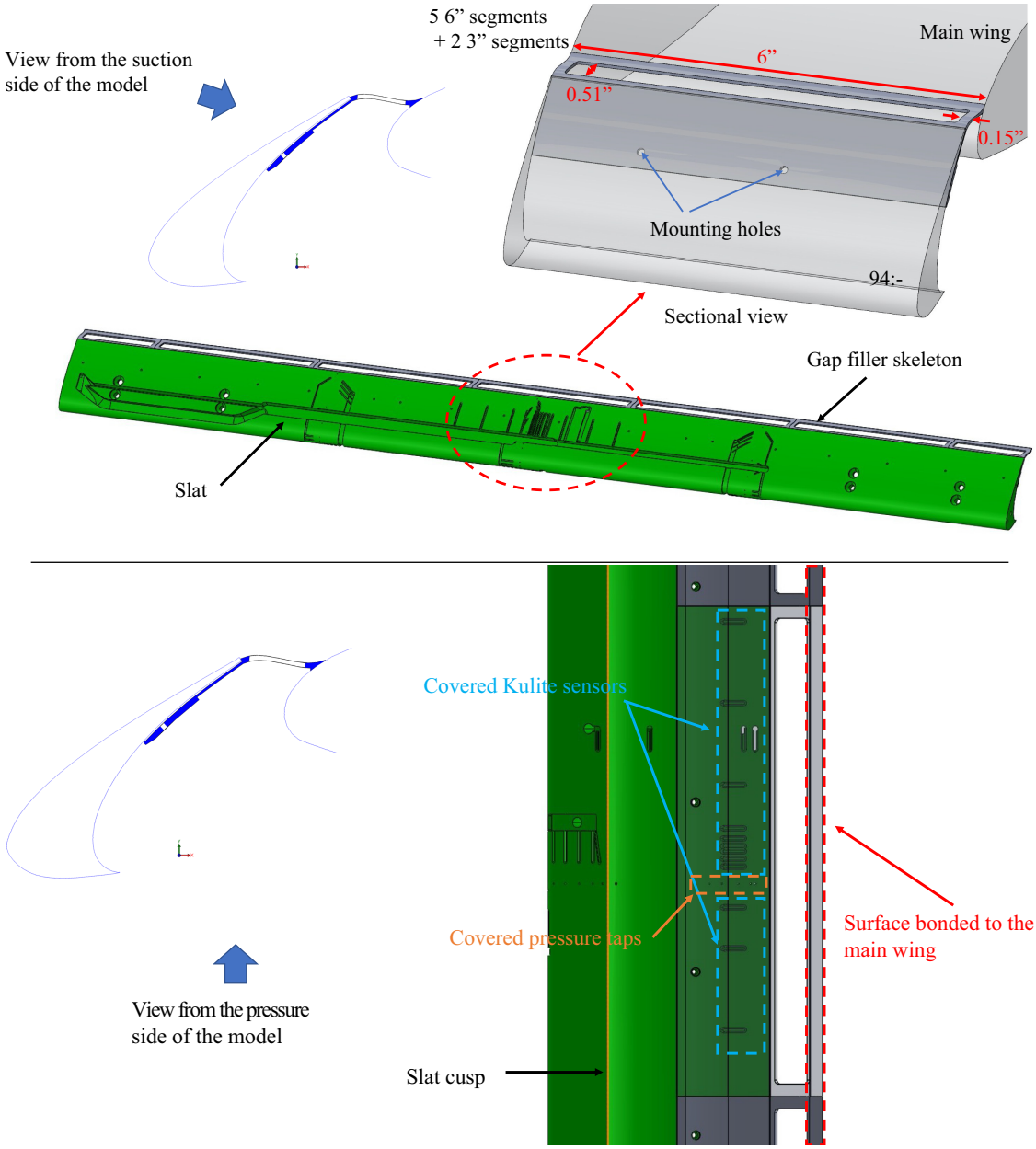

Fig. 2 CAD drawing details of the gap filler skeleton.

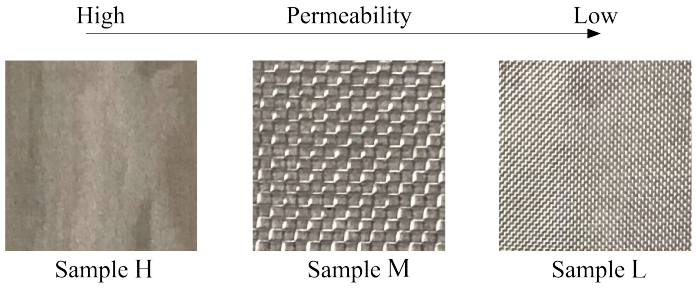

Fig. 3 Pictures of three porous samples.

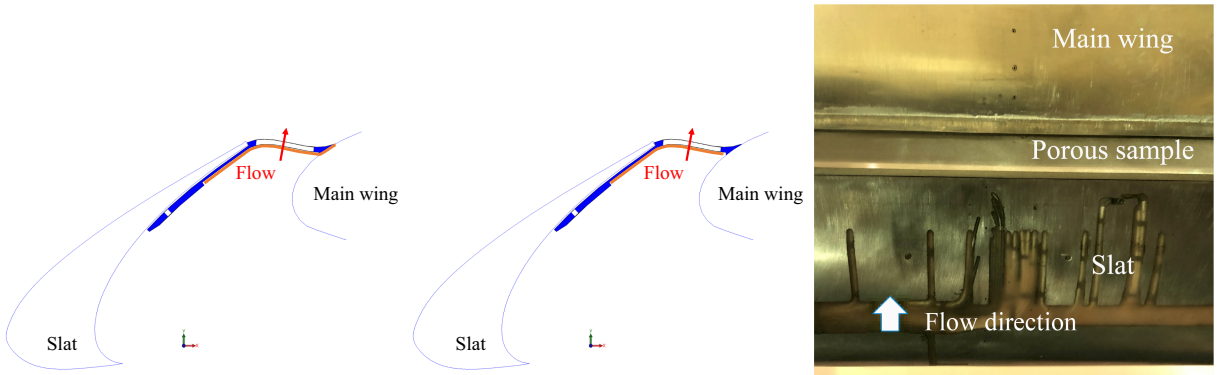

(a) Installation of sample H **(b) Installation of sample M or L** **(c) Picture of installed sample H**

Fig. 4 Installation of porous samples.

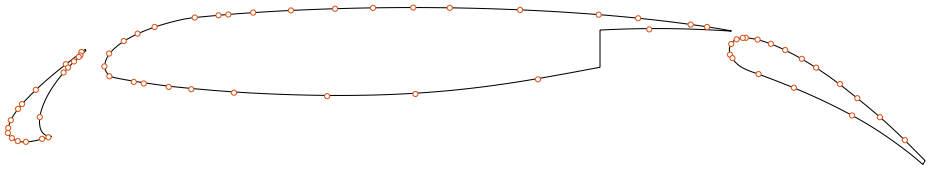

Fig. 5 Location of steady pressure taps on the 30P30N airfoil surface [26].

of the airfoil in order to measure the radiated sound in a flyover configuration. During the measurements, the pitot probe located 0.9 m upstream is traversed out of the test section to avoid corrupting the acoustic data. The microphone data are simultaneously sampled at 204.8 kHz over a duration of 60 seconds by using multiple NI 4462 (24-bit) cards installed in the PXI 1045 chassis. Prior to the measurements, the sensitivity of each microphone was calibrated against a Brüel and Kjær pistonphone (Type 4220) at 250 Hz. An acoustic correction due to the transmission through the Kevlar wall is also applied [7]. The DAS beamforming is applied to visualize the noise source maps. The spatial resolution is poor at low frequencies (< 1 kHz), with the 3-dB beamwidth being greater than 0.6 m. As the frequency is increased, the resolution is improved, but the number of potential false sources also increases due to an increased number of sidelobes [7].

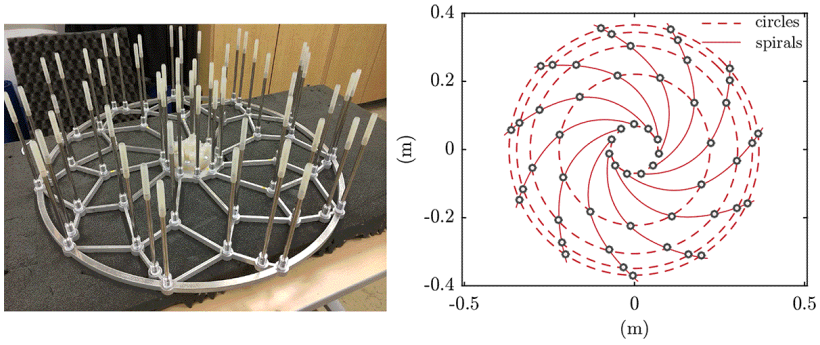

Fig. 6 Microphone array skeletal frame (left) and layout showing design criteria (right) [7].

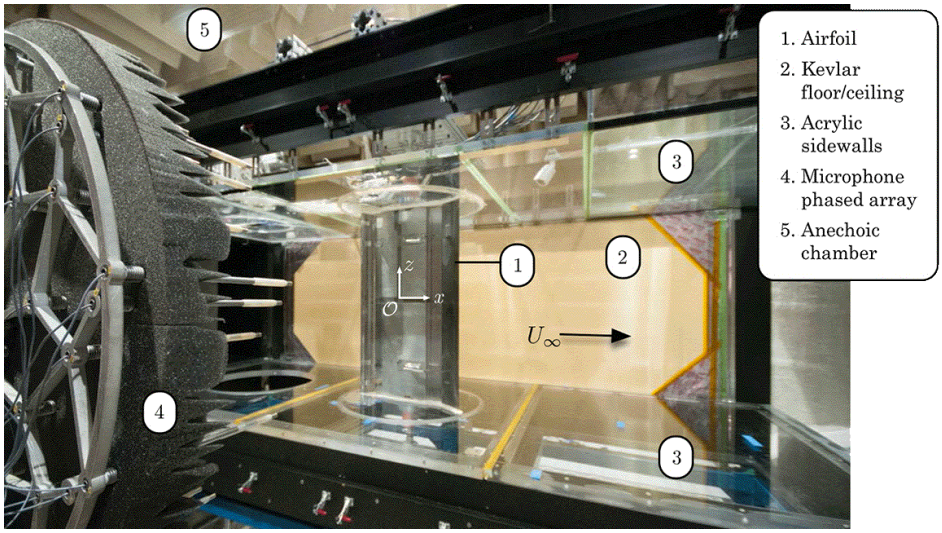

Fig. 7 Image of far-field acoustic measurement setup [7]. The Kevlar wall between the airfoil and the acoustic array is not shown in the picture.

III. Results and discussion

A. Steady surface pressure distribution

Due to similarities among the results for the three Reynolds numbers, only the results at the highest Reynolds number (i.e., $Re_c = 1.71 \times 10^6$) are given in Figure 8, along with the baseline values without the gap filler. The least permeable gap filler corresponding to porous sample L results in a similar C_p signature as the previous solid gap filler case. The aerodynamics are significantly changed with increasing permeability. Noticeable aerodynamic degradation is observed for samples H and M as the pressure increases on the suction side of the model. This indicates that flow separation may occur due to the flow through the porous gap filler. The degradation is also observed further downstream on the flap. The pressure distribution on the pressure side is weakly affected. As in the previous solid gap filler case, some pressure ports on the slat cove surface are covered by the gap filler skeleton. Therefore, only the lift coefficient on the main wing and the flap can be calculated and are presented in Figure 9. It is clear that the aerodynamic performance degrades with the increase in permeability. It should also be noted that the effective free-air AoA with the gap fillers could be different than the basline case, which means the 2.5° angle correction may not hold for the gap filler cases.

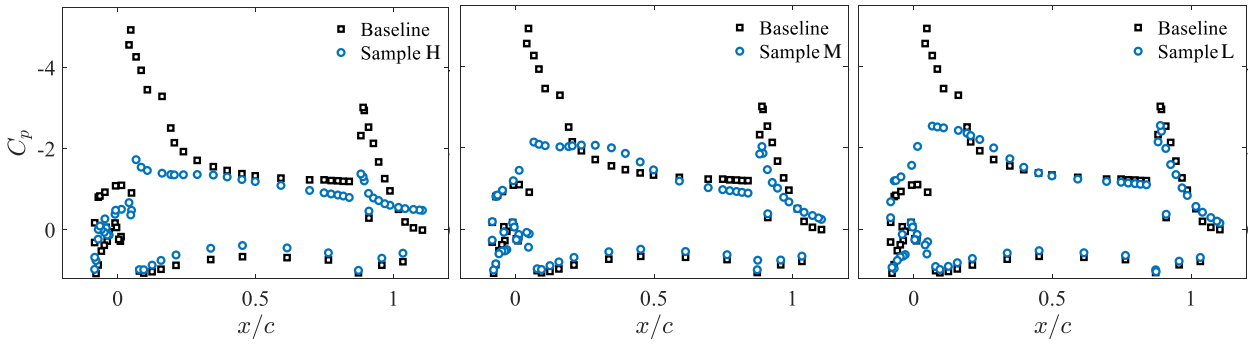

(a) sample H **(b) sample M** **(c) sample L**

Fig. 8 C_p distribution for three porous samples at the Reynolds number of 1.71×10^6. The permeability of samples decreases from sample H to sample L.

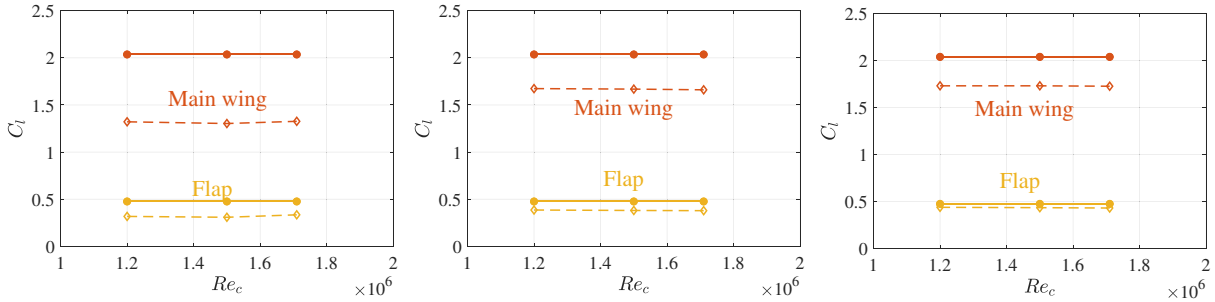

(a) sample H **(b) sample M** **(c) sample L**

Fig. 9 C_l distribution for three porous samples at the Reynolds number of 1.71×10^6. The solid lines represent baseline cases, and the dashed lines represent porous sample cases. The permeability of samples decreases from sample H to sample L.

B. Unsteady surface pressure

The normalized autospectra of surface pressure fluctuations for the three porous gap filler cases are shown in Figure 10. For sample H, the surface pressure fluctuations are significantly reduced at the P_3 location, with the exception of a new peak in the P_3 spectra at $St_s = 0.1$ at $Re_c = 1.2 \times 10^6$. However, this peak nearly disappears at the higher Reynolds numbers. The sample M case exhibits different pressure signature at P_3. There are two mild peaks showing up between $St_s = 0.1$ and 0.3, and broadband contents are slightly higher than the baseline. At the sensor location close to the trailing edge (sensor P_6), the pressure fluctuations are similar for all three samples. The narrowband peaks introduced by the slat-cove shear layer are suppressed, similar to the solid gap filler case. The broadband content below $St_s = 1$ in the P_6 spectrum is slightly higher for the sample H below $St_s = 1$. These observations indicate that the flow features in the sample H case can be quite different from samples M and L.

C. Beamforming maps and integrated sound pressure level

The source maps for the porous gap fillers at $Re_c = 1.71 \times 10^6$ are compared in Figure 11. These source maps are selected at the narrowband frequencies observed in the baseline case. For sample H, the dominant noise sources are clearly located along the slat region. For samples M and L, the level of dominant noise sources (except for $St_s = 1.38$) is reduced and shifted further downstream to the flap region, similar to the solid gap filler case. This suggests that the noise reduction mechanism of samples M and L is possibly similar to the solid gap filler that the shear layer trajectory is altered resulting in a disruption of the acoustic feedback loop. As sample H has the highest permeability, a larger amount of fluid can pass through the porous media. In this condition, the shear layer trajectory is expected to be somewhere between the baseline and the solid gap filler cases. However, without flow field visualization, the accurate shear layer characteristics cannot be determined. Thus, the noise reduction mechanism remains unknown at this stage.

In order to assess the far-field acoustic spectra, the integrated sound pressure levels (SPLs) in region I_1 (defined in Figure 12) for the different porous samples are compared with the corresponding baseline cases in Figure 13. For samples M and L, the noise reduction effects are similar to each other for $St_s < 10$ in that a significant suppression of noise is observed for both broadband and narrowband. Sample H suppresses the original narrowband peaks induced by the slat-cove shear layer while barely affecting the broadband noise. The noise reduction performance is assessed by calculating the overall sound pressure level (OASPL), and the results are compiled in Table 3. The sample H gap filler can achieve approximately 5 dB noise reduction, which is much less compared with the 10 dB reduction enabled via samples M and L.

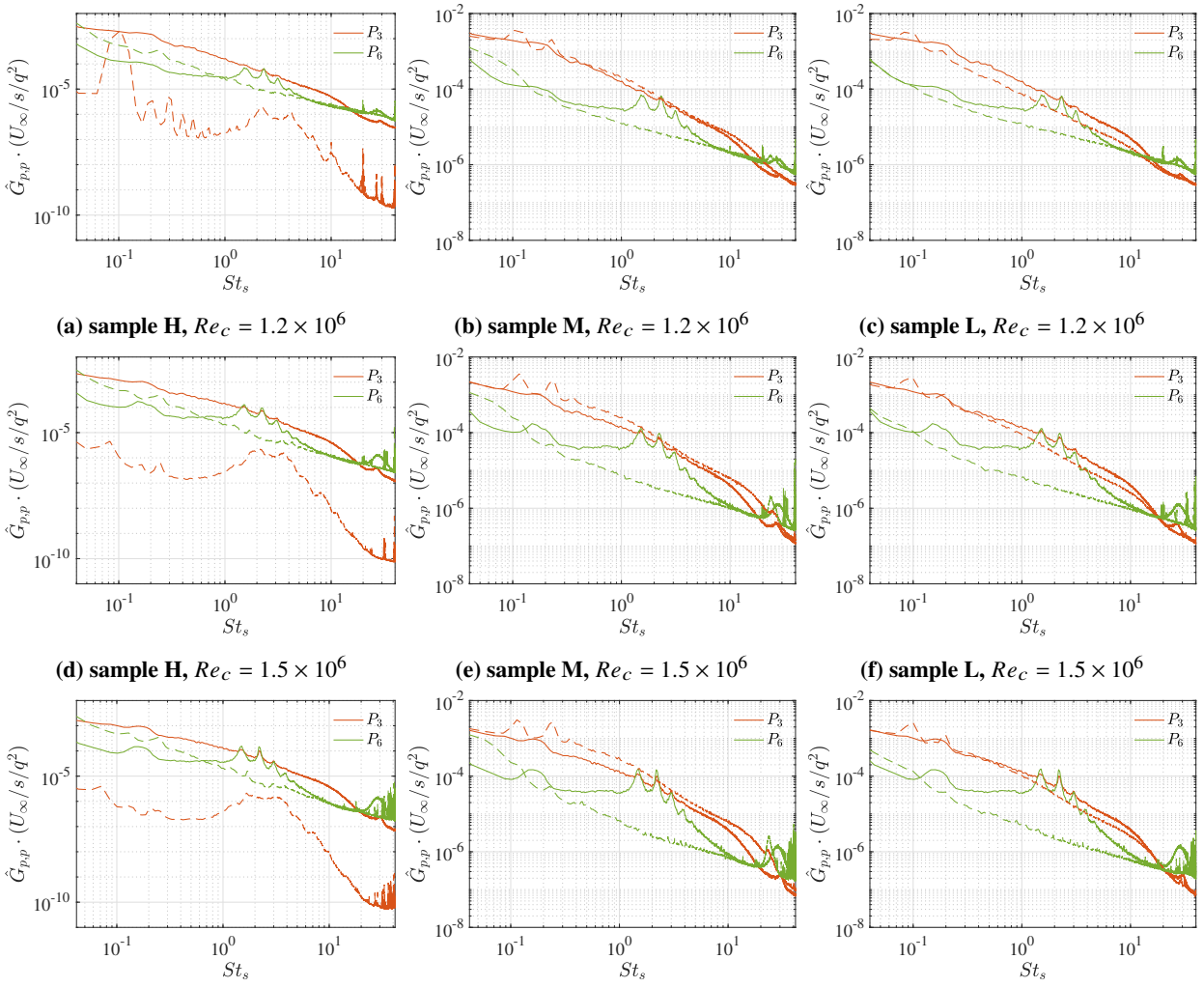

(a) sample H, $Re_c = 1.2 \times 10^6$ **(b) sample M,** $Re_c = 1.2 \times 10^6$ **(c) sample L,** $Re_c = 1.2 \times 10^6$

(d) sample H, $Re_c = 1.5 \times 10^6$ **(e) sample M,** $Re_c = 1.5 \times 10^6$ **(f) sample L,** $Re_c = 1.5 \times 10^6$

(g) sample H, $Re_c = 1.71 \times 10^6$ **(h) sample M,** $Re_c = 1.71 \times 10^6$ **(i) sample L,** $Re_c = 1.71 \times 10^6$

Fig. 10 Spectra of surface fluctuating pressure for the porous gap filler cases at $\alpha_k = 8°$. Solid and dashed lines represent the baseline and treatment cases, respectively. Permeability decreases from sample H to L.

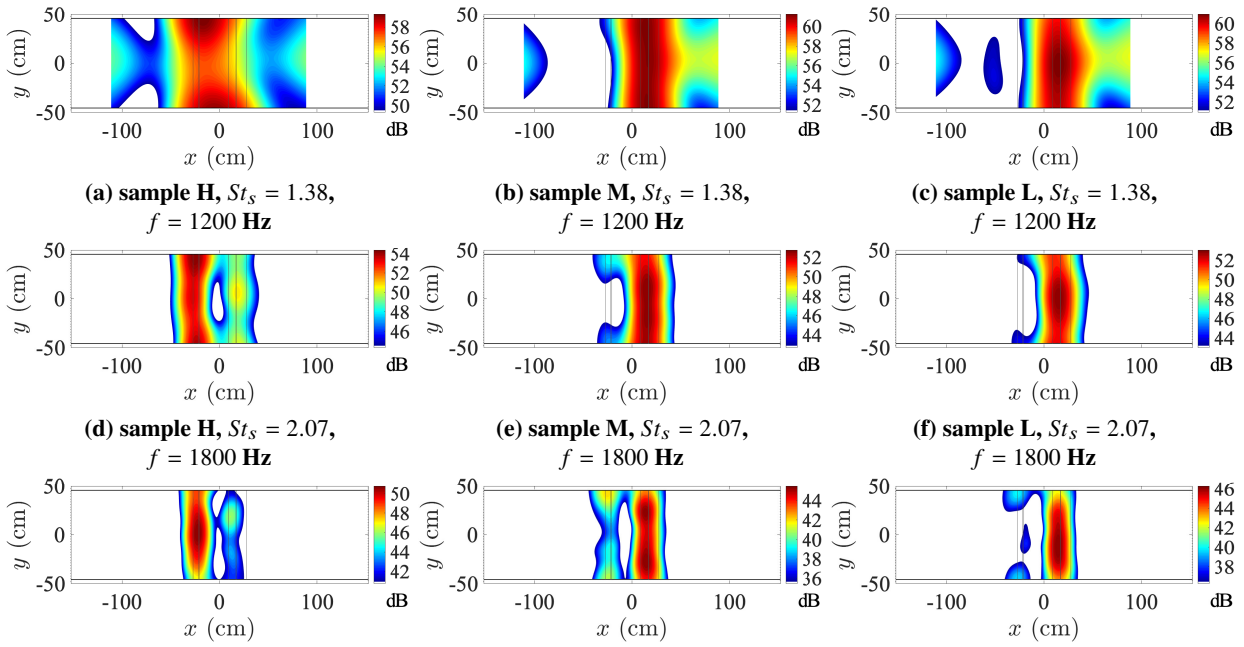

(a) sample H, St_s = 1.38, f = 1200 Hz **(b) sample M, St_s = 1.38, f = 1200 Hz** **(c) sample L, St_s = 1.38, f = 1200 Hz**

(d) sample H, St_s = 2.07, f = 1800 Hz **(e) sample M, St_s = 2.07, f = 1800 Hz** **(f) sample L, St_s = 2.07, f = 1800 Hz**

(g) sample H, St_s = 2.84, f = 2472 Hz **(h) sample M, St_s = 2.84, f = 2472 Hz** **(i) sample L, St_s = 2.84, f = 2472 Hz**

Fig. 11 Source maps of porous gap filler cases for $\alpha_k = 8°$ at $Re_c = 1.71 \times 10^6$ for narrowband DAS with 10 dB dynamic range relative to peak level. The center frequencies correspond to the first three slat-cove shear layer modes. The flow direction is from left to right. The vertical lines present the projection of the model outlines.

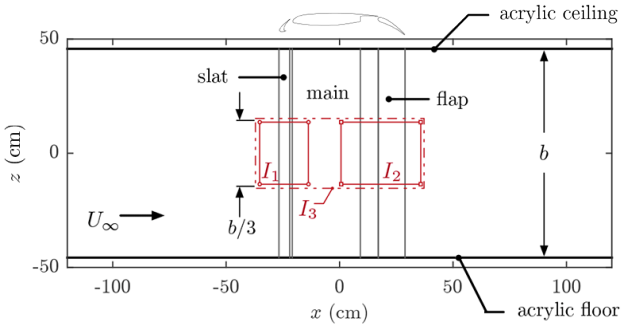

Fig. 12 Definition of integration region [7].

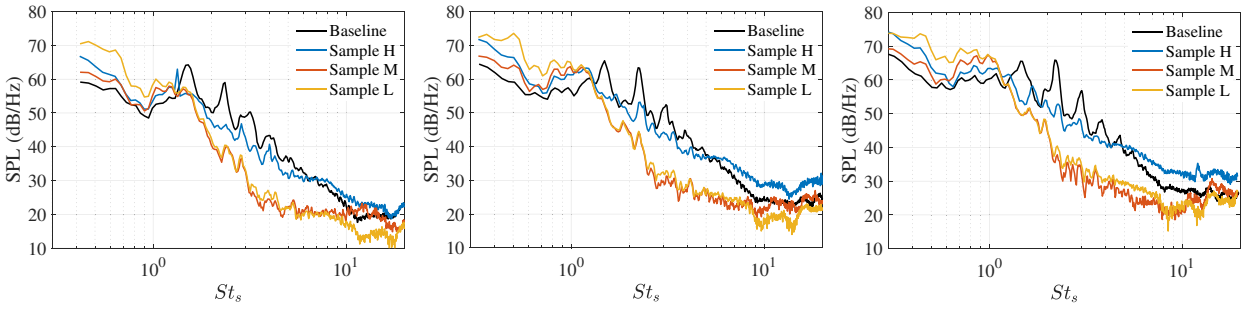

(a) $Re_c = 1.2 \times 10^6$ **(b) $Re_c = 1.5 \times 10^6$** **(c) $Re_c = 1.71 \times 10^6$**

Fig. 13 Comparison of integrated sound pressure spectra between baseline and three porous samples from region I_1 in the Kevlar test section. The sound pressure levels are scaled to a 1 m span at 1 m observer distance.

Table 3 Difference of OASPL (dB) compared with baseline case for the porous gap filler cases.

Re_c	1.2×10^6	1.5×10^6	1.71×10^6
sample H	-5.1	-5.6	-4.7
sample M	-10.6	-11.1	-9.8
sample L	-11.7	-11.2	-9.7

IV. Conclusions

The current research has continued our previous study [16] on passive control devices to reduce the slat noise from a high-lift airfoil system. In extending our previously reported measurements for the solid gap filler concept, we have investigated the effectiveness of three porous gap fillers that allow increasing amounts of flow through the slat gap. The steady pressure measurements confirm the degradation in aerodynamic performance with increasing permeability. In particular, the sample H gap filler with the highest permeability lost lift on both the main wing and the flap, which may be due to a flow separation on the suction side of the model. Flow visualization on the suction side of the model would help elucidate the flow physics underlying the significant aerodynamic degradation. The beamforming source maps show that the slat noise level is still dominant for the sample H, whereas the dominant noise source shifts further downstream to the flap region for samples M and L with the medium and low levels of permeability, respectively. A comparison of the integrated SPLs for the three samples shows that the samples M and L suppress both narrowband peaks and the broadband noise, similar to the nonporous gap filler. On the other hand, the sample H suppresses only the narrowband peaks and has a rather weak influence on the broadband level. At high frequencies, the broadband noise even increases for the sample H case. The noise reduction mechanism of samples M and L is presumably similar to taht of the solid (i.e., nonporous) gap filler. The details of the flow physics associated with the differences among the different porous gap fillers are investigated in Part II.

Acknowledgement

This research was supported by NASA under contract 80NSSC18P3447. The authors gratefully acknowledge the NASA Langley, FCAAP, and MagLab machine shops for the fabrication of the noise control treatments.

References

[1] Dobrzynski, W., "Almost 40 Years of Airframe Noise Research: What Did We Achieve?" *Journal of Aircraft*, Vol. 47, 2010, pp. 353–367. https://doi.org/10.2514/1.44457.

[2] Khorrami, M. R., Berkman, M. E., and Choudhari, M., "Unsteady Flow Computations of a Slat with a Blunt Trailing Edge," *AIAA Journal*, Vol. 38, No. 11, 2000, pp. 2050–2058. https://doi.org/10.2514/3.14649.

[3] Singer, B. A., Lockard, D. P., and Brentner, K. S., "Computational Aeroacoustic Analysis of Slat Trailing-Edge Flow," *AIAA Journal*, Vol. 38, No. 9, 2000, pp. 1558–1564. https://doi.org/10.2514/3.14581.

[4] Khorrami, M. R., Singer, B. A., and Berkman, M. E., "Time-Accurate Simulations and Acoustic Analysis of Slat Free Shear Layer," *AIAA Journal*, Vol. 40, 2002, pp. 1284–1291. https://doi.org/10.2514/3.15195.

[5] Choudhari, M., Lockard, D., Macaraeg, M., Singer, B., Streett, C., Neubert, G., Stoker, R., Underbrink, J., Berkman, M., Khorrami, M., and Sadowski, S., "Aeroacoustic Experiments in the Langley Low-Turbulence Pressure Tunnel," Tech. rep., NASA, 2002. TM 2002-211432.

[6] Terracol, M., Manoha, E., and Lemoine, B., "Investigation of the Unsteady Flow and Noise Generation in a Slat Cove," *AIAA Journal*, Vol. 54, No. 2, 2016, pp. 469–489. https://doi.org/10.2514/1.j053479.

[7] Pascioni, K., "An Aeroacoustic Characterization of a Multi-Element High-Lift Airfoil," Ph.D. thesis, Florida State University, Tallahassee, FL, 2017.

[8] Rossiter, J. E., "Wind-tunnel Experiments on the Flow over Rectangular Cavities at Subsonic and Transonic Speeds," Tech. rep., Aeronautical Research Council Reports and Memoranda, 1964. No. 3438.

[9] Pascioni, K. A., and Cattafesta, L. N., "Unsteady Characteristics of a Slat-Cove Flow Field," *Phys. Rev. Fluids*, Vol. 3, 2018. https://doi.org/10.1103/PhysRevFluids.3.034607.

[10] Choudhari, M. M., and Khorrami, M. R., "Effect of Three-Dimensional Shear-Layer Structures on Slat Cove Unsteadiness," *AIAA Journal*, Vol. 45, No. 9, 2007, pp. 2174–2186. https://doi.org/10.2514/1.24812.

[11] Knacke, T. J., and Thiele, F., "Numerical Analysis of Slat Noise Generation," *19th AIAA/CEAS Aeroacoustics Conference*, American Institute of Aeronautics and Astronautics, Reston, Virginia, 2013. https://doi.org/10.2514/6.2013-2162, AIAA Paper 2013-2162.

[12] Dobrzynski, W., Gehlhar, B., and Buchholz, H., "Model and full scale high-lift wing wind tunnel experiments dedicated to airframe noise reduction," *Aerospace Science and Technology*, Vol. 5, No. 1, 2001, pp. 27–33. https://doi.org/10.1016/s1270-9638(00)01079-8.

[13] Bridges, J., and Brown, C., "Parametric Testing of Chevrons on Single Flow Hot Jets," *10th AIAA/CEAS Aeroacoustics Conference*, American Institute of Aeronautics and Astronautics, 2004. https://doi.org/10.2514/6.2004-2824, AIAA Paper 2004-2824.

[14] Khorrami, M. R., and Lockard, D. P., "Effects of Geometric Details on Slat Noise Generation and Propagation," *International Journal of Aeroacoustics*, Vol. 9, No. 4-5, 2010, pp. 655–678. https://doi.org/10.1260/1475-472X.9.4-5.655.

[15] Kopiev, V., Zaitsev, M., Belyaev, I., and Mironov, M., "Noise Reduction Potential through Slat Hook Serrations," *17th AIAA/CEAS Aeroacoustics Conference (32nd AIAA Aeroacoustics Conference)*, American Institute of Aeronautics and Astronautics, 2011. https://doi.org/10.2514/6.2011-2909, AIAA Paper 2011-2909.

[16] Zhang, Y., ONeill, A., Cattafesta, L. N., Pascioni, K., Choudhari, M., Khorrami, M. R., Lockard, D. P., and Turner, T., "Assessment of Noise Reduction Concepts for Leading-Edge Slat Noise," *2018 AIAA/CEAS Aeroacoustics Conference*, American Institute of Aeronautics and Astronautics, 2018. https://doi.org/10.2514/6.2018-3461, AIAA Paper 2018-3461.

[17] Horne, W., James, K., Arledge, T., Soderman, P., Burnside, N., and Jaeger, S., "Measurements of 26%-Scale 777 Airframe Noise in the NASA Ames 40- by 80 Foot Wind Tunnel," *11th AIAA/CEAS Aeroacoustics Conference*, American Institute of Aeronautics and Astronautics, 2005. https://doi.org/10.2514/6.2005-2810, AIAA Paper 2005-2810.

[18] Imamura, T., Ura, H., Yokokawa, Y., Enomoto, S., Yamamoto, K., and Hirai, T., "Designing of Slat Cove Filler as a Noise Reduction Device for Leading-edge Slat," *13th AIAA/CEAS Aeroacoustics Conference (28th AIAA Aeroacoustics Conference)*, American Institute of Aeronautics and Astronautics, 2007. https://doi.org/10.2514/6.2007-3473, AIAA Paper 2007-3473.

[19] Jawahar, H. K., Azarpeyvand, M., and Ilario, C., "Experimental Investigation of Flow Around Three-Element High-Lift Airfoil with Morphing Fillers," *23rd AIAA/CEAS Aeroacoustics Conference*, American Institute of Aeronautics and Astronautics, 2017. https://doi.org/10.2514/6.2017-3364, AIAA Paper 2017-3364.

[20] Arena, G., Groh, R., Pirrera, A., Scholten, W., Hartl, D., and Turner, T., "A Tailored Nonlinear Slat-Cove Filler for Airframe Noise Reduction," *Volume 1: Development and Characterization of Multifunctional Materials; Modeling, Simulation, and Control of Adaptive Systems; Integrated System Design and Implementation*, American Society of Mechanical Engineers, 2018. https://doi.org/10.1115/smasis2018-8079.

[21] Herr, M., Pott-Pollenske, M., Ewert, R., Boenke, D., Siebert, J., Delfs, J., Rudenko, A., Büscher, A., Friedel, H., and Mariotti, I., "Large-Scale Studies on Slat Noise Reduction," *21st AIAA/CEAS Aeroacoustics Conference*, American Institute of Aeronautics and Astronautics, 2015. https://doi.org/10.2514/6.2015-3140, AIAA Paper 2015-3140.

[22] Turner, T. L., and Long, D. L., "Development of a SMA-Based, Slat-Gap Filler for Airframe Noise Reduction," *23rd AIAA/AHS Adaptive Structures Conference*, American Institute of Aeronautics and Astronautics, Reston, Virginia, 2015. https://doi.org/10.2514/6.2015-0730, AIAA Paper 2015-0730.

[23] Pagani, C. C., Souza, D. S., and Medeiros, M. A., "Experimental investigation on the effect of slat geometrical configurations on aerodynamic noise," *Journal of Sound and Vibration*, Vol. 394, 2017, pp. 256–279. https://doi.org/10.1016/j.jsv.2017.01.013.

[24] Lu, W., Liu, P., and Guo, H., "Experimental Study on Comparison on Noise Characteristics of Noise Reduction Leading-edge Slats," *25th AIAA/CEAS Aeroacoustics Conference*, American Institute of Aeronautics and Astronautics, 2019. https://doi.org/10.2514/6.2019-2404, AIAA 2019-2404.

[25] Zhang, Y., Richardson, R., Cattafesta, L. N., Pascioni, K., Choudhari, M., Khorrami, M. R., Lockard, D. P., and Turner, T., "Slat Noise Control Using a Slat Gap Filler," *AIAA AVIATION 2020 FORUM*, American Institute of Aeronautics and Astronautics, 2020. https://doi.org/https://doi.org/10.2514/6.2020-2553, AIAA Paper 2020-2553.

[26] Zhang, Y., Cattafesta, L. N., Pascioni, K. A., Choudhari, M. M., Khorrami, M. R., Lockard, D. P., and Turner, T., "Assessment of Slat Extensions and a Cove Filler for Slat Noise Reduction," *AIAA Journal*, Vol. 59, No. 12, 2021, pp. 4987–5000. https://doi.org/10.2514/1.j060502.

[27] Pascioni, K., Reger, R., Edstrand, A., and Cattafesta, L., "Characterization of an Aeroacoustic Wind Tunnel Facility," *43rd International Congress on Noise Control Engineering*, Vol. 249, 2014, pp. 3966–3975.

[28] Choudhari, M. M., Bahr, C., Khorrami, M. R., Lockard, D. P., Lopes, L., Zawodny, N., Herr, M., Pott-Pollenske, M., Kamruzzaman, M., Van de Ven, T., Manoha, E., Redonnet, S., Yamamoto, K., Ikeda, I., and Imamura, T., "Simulation & Measurement of Airframe Noise: A BANC Workshops Perspective," *Proceedings of NATO STO-MP-AVT-246 Specialists Meeting on Progress and Challenges in Validation Testing for Compuatational Fluid Dynamics*, Avila, Spain, 2016.

[29] Choudhari, M. M., and Lockard, D. P., "Assessment of Slat Noise Predictions for 30P30N High-Lift Configuration from BANC-III Workshop," *21st AIAA/CEAS Aeroacoustics Conference*, American Institute of Aeronautics and Astronautics, Reston, Virginia, 2015. https://doi.org/doi:10.2514/6.2015-2844, AIAA Paper 2015-2844.

[30] Choudhari, M. M., Lockard, D. P., Khorrami, M. R., and Mineck, R. E., "Slat Noise Simulations: Status and Challenges," *Inter-Noise 2011*, Osaka, Japan, 2011.

[31] Reger, R., Zawodny, N., Pascioni, K., Wetzel, D., Liu, F., and Cattafesta, L., "Design-Optimization of a Broadband Phased Microphone Array for Aeroacoustic Applications," *Journal of the Acoustical Society of America*, Vol. 131, 2012. https://doi.org/10.1121/1.4708011.